Analysis of density effects in plasmas and their influence on electron-impact cross sections

M. Belkhiri and M. Poirier*

CEA, IRAMIS, Laboratoire Interactions, Dynamique et Lasers, Centre d'Études de Saclay, F91191 Gif-sur-Yvette Cedex, France

(Received 18 March 2014; revised manuscript received 21 July 2014; published 24 December 2014)

Density effects in plasmas are analyzed using a Thomas-Fermi approach for free electrons. First, scaling properties are determined for the free-electron potential and density. For hydrogen-like ions, the first two terms of an analytical expansion of this potential as a function of the plasma coupling parameter are obtained. In such ions, from these properties and numerical calculations, a simple analytical fit is proposed for the plasma potential, which holds for any electron density, temperature, and atomic number, at least assuming that Maxwell-Boltzmann statistics is applicable. This allows one to analyze perturbatively the influence of the plasma potential on energies, wave functions, transition rates, and electron-impact collision rates for single-electron ions. Second, plasmas with an arbitrary charge state are considered, using a modified version of the Flexible Atomic Code (FAC) package with a plasma potential based on a Thomas-Fermi approach. Various methods for the collision cross-section calculations are reviewed. The influence of plasma density on these cross sections is analyzed in detail. Moreover, it is demonstrated that, in a given transition, the radiative and collisional-excitation rates are differently affected by the plasma density. Some analytical expressions are proposed for hydrogen-like ions in the limit where the Born or Lotz approximation applies and are compared to the numerical results from the FAC.

DOI: 10.1103/PhysRevA.90.062712 PACS number(s): 34.80.Dp, 52.20.Fs, 52.25.−b, 52.27.Gr

I. INTRODUCTION

In a number of cases such as in inertial confinement devices and in stellar interiors the ions in plasmas cannot be considered isolated. The environment in plasmas plays a significant role at high density, leading to level polarization, pressure-induced ionization, and changes in absorption or emission spectra and in the equation of state [1–3]. To model such effects the first attempts were done using the Debye-Hückel theory [4], but its perturbative nature limits its applicability to low-density or high-temperature plasmas. A series of other approaches has been developed, most of them based on the ion-sphere model for plasma, which assumes spherical symmetry and neutrality inside the Wigner sphere [5], and define a local free-electron density from self-consistency equations. These theories may be based on Thomas-Fermi (TF) [6], relativistic TF [7], hypernetted chain networks [8], and, more generally, density functional theories [9]. Some approaches provide a fully quantum mechanical description of the free electrons [10–12]. A very popular model for level shifts which makes the connection between low and high densities has been developed by Stewart and Pyatt [13]. However this model assumes thermal equilibrium for ions as well as electrons and, therefore, is not directly usable in the analysis of plasmas out of local thermal equilibrium. A simplified form of the ion-sphere model, valid at high temperatures, is the uniform electron gas model (UEGM), which assumes a uniform free-electron density inside the Wigner sphere [14]. At variance with the previous approach, this model does not rely on thermal equilibrium conditions.

In a previous paper [15], we have shown that we may use a formalism based on the UEGM to describe the plasma environment effect on energies and wave functions. This has been done first in the hydrogenic case, leading to analytical energies and radial matrix elements at first perturbation order. Then such effects have been included in a more realistic way by including a plasma potential contribution in the Flexible Atomic Code (FAC) [16], which is widely used in the community of atomic physics in plasmas. Conversely, many analyses of plasma effects on atomic structure available in the literature use a Hartree-Fock formalism [17] or, in simpler cases, a hydrogen-like framework [18,19]. In Ref. [15] we limited the analysis to the high-temperature case and to the analysis of energies and radiative rates. However, collisional cross sections deserve special interest for at least two reasons. First, in order to describe plasmas out of local thermodynamical equilibrium, it is necessary to solve kinetic equations which involve the radiative and collisional transition rates. Second, the lineshape determination, particularly important for spectral opacity calculation, requires a detailed analysis of collisional rates (see, e.g., [20]). Most of the available literature on plasma effects on excitation cross sections rely on the Debye-Hückel potential [21–25] or on the UEGM [24]. Ionization impact cross sections are also dealt with in a series of papers, based on the Debye-Hückel hypothesis [23,25,26] or TF approach [27]. But to our knowledge, such an analysis has not yet been performed using a relativistic parametric potential code such as the FAC.

This paper is organized as follows. First, we review the TF theory for free electrons, for which we formulate scaling properties with respect to density, temperature, and charge, and provide the first two terms in the plasma-coupling-parameter expansion in the case of hydrogen-like ions. For such ions, we then mention a simple analytical expression of the plasma potential valid for a wide range of temperatures and densities. Next, we propose comparisons between the UEGM and the TF theory regarding energies and radiative rates. Then we analyze the plasma influence on excitation and ionization cross sections for complex ions. To confirm

*michel.poirier@cea.fr

the numerical predictions of plasma effects obtained with the FAC, semiempirical calculations using an analytical approach for hydrogenic ions are compared to numeric calculations. Concluding remarks are finally given.

II. DETERMINATION OF THE PLASMA POTENTIAL

A. Theory

The self-consistent equations defining the free-electron density and the plasma potential in a semiclassical picture—TF restricted to free electrons—has been discussed in a series of papers [18,28]. In the ion-sphere theory [5], neutrality is assumed inside a Wigner sphere with radius R_0 defined by

$$4\pi R_0^3 N_e/3 = Z_f = Z - N_b, \tag{1}$$

where N_e is the average electron density, Z is the nuclear charge, N_b the number of bound electrons, and Z_f the ionic net charge. The free-electron and other-ion background densities are supposed to neutralize $n_e(r) = 0$ for $r \geqslant R_0$. In order to comply with the definition of the average density N_e, one imposes

$$4\pi \int_0^{R_0} dr\ r^2 n_e(r) = Z_f. \tag{2}$$

Assuming Maxwell-Boltzmann statistics, the free-electron density follows

$$n_e(r) \propto \int_{p_0(r)}^{\infty} dp\ p^2 \exp\left(-\left(\frac{p^2}{2m} + V(r)\right) \Big/ kT_e \right), \tag{3}$$

where m and T_e are the electron mass and temperature, respectively, k is the Boltzmann constant, and $p_0(r)$ is the minimal momentum value making the total electron energy positive; i.e., $p_0(r) = (-2mV(r))^{1/2}$ if $V(r) \leqslant 0$ or 0 if $V(r) > 0$. Here we assume thermal equilibrium for electrons but not necessarily for ions. The quantity $V(r)$ is the energy associated with the electrostatic interaction with all the charges included in the Wigner sphere, namely, the nucleus, bound electrons, and free electrons:

$$V(r) = -\frac{Ze^2}{r} + V_b(r) + V_{\rm pl}(r). \tag{4}$$

Hereafter we use the word "potential," which implies "potential energy," not electrostatic potential, the former being $-e$ times the latter. For multielectron ions, one must note that the bound-free interaction $V_b(r)$ depends on the ion bound-electron wave function and, therefore, changes as the ion excitation changes. The term $V_{\rm pl}(r)$ describing the interaction with free electrons is the so-called plasma potential. Fermi-Dirac statistics is usually not necessary as shown by the analysis proposed in the Appendix. We also assume that free electrons are not relativistic, which holds for temperatures $kT_e \ll 511$ keV, which is always fulfilled in the cases considered here. Starting in Sec. V, we consider the general case of multielectron ions where $V_b(r)$ is derived from an atomic model. In this part, to derive general properties of the plasma potential, we mainly consider hydrogen-like ions where the V_b term is absent.

The last equation required to obtain the plasma potential and the electron density is the Poisson equation, which can be written in integral form:

$$V_{\rm pl}(r) = 4\pi e^2 \left(\frac{1}{r} \int_0^r ds\ s^2 n_e(s) + \int_r^{R_0} ds\ s n_e(s) \right). \tag{5}$$

This expression ensures that $V_{\rm pl}(r)$ and its derivative are continuous at $r = R_0$, knowing that $V_{\rm pl}(r) = Z_f e^2/r$ if $r \geqslant R_0$, according to the ion-sphere hypothesis.

Assuming an attractive potential $V(r) < 0$, the Maxwell-Boltzmann equation, (3), leads to

$$n_e(r) = \frac{K}{2} e^{-V(r)/kT_e} (2mkT_e)^{3/2} \Gamma\left(\frac{3}{2}, -\frac{V(r)}{kT_e}\right) \tag{6a}$$

$$= \frac{K}{2} (2mkT_e)^{3/2} \left[\left(-\frac{V(r)}{kT_e} \right)^{1/2} + \frac{\pi^{1/2}}{2} e^{-V(r)/kT_e} \operatorname{erfc}\left(\left(-\frac{V(r)}{kT_e} \right)^{1/2} \right) \right], \tag{6b}$$

the constant K being derived from the neutrality condition, (2). We have introduced the incomplete Γ function $\Gamma(a,x) = \int_x^{\infty} dt\ t^{a-1} e^{-t}$ and the complementary error function $\operatorname{erfc}(x) = (2/\pi^{1/2}) \int_x^{\infty} du\ e^{-u^2}$ [29].

B. Numerical method

The plasma potential and free-electron density are numerically obtained from an efficient iterative scheme. Starting from the UEGM solution

$$n_e(r) = N_e, \tag{7a}$$

$$V_{\rm UEGM} = \frac{Z_f e^2}{2R_0} \left(3 - \frac{r^2}{R_0^2} \right) \tag{7b}$$

for $r \leqslant R_0$, one obtains a first iteration for the density using the Maxwell-Boltzmann equation, (6a)—where the overall constant is determined by the neutrality condition—and a first-order iterated potential using the Poisson equation, (5). One next obtains the second-order electron density and plasma potential. The convergence is controlled by monitoring the variation of the density on the Wigner sphere $|n_e^{(i+1)}(R_0) - n_e^{(i)}(R_0)|$, ending iteration when this difference falls below a given ε. We found that $\varepsilon = 10^{-8}$ in atomic units gave the self-consistent potential with a fair accuracy and that the procedure converged in most cases in fewer than 12 iterations.

C. Calculations of free-electron density and plasma potential in H-like ions

In Fig. 1 is plotted the free-electron density in units of the average value N_e using Maxwell-Boltzmann statistics in H-like helium $Z = 2$, $Z_f = 1$. From bottom to top the curves correspond to $T_e = 500$, 5000, 5, and 0.005 eV, respectively. The free-electron density is 10^{12} per cm^3 for the lowest curve and 10^{21} cm^{-3} for the three others. Defining a radius connected to the electron temperature (up to a $1/\pi$ factor, this is the closest-approach distance),

$$R_1 = \frac{Z_f e^2}{\pi k T_e}, \tag{8}$$

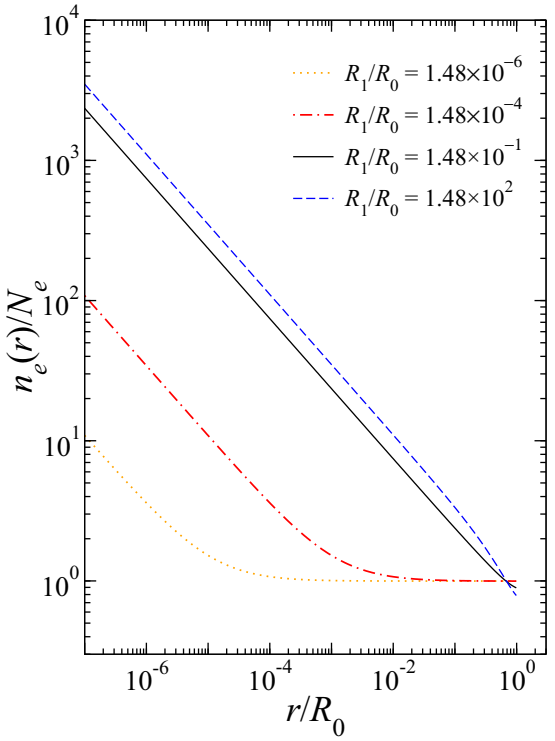

FIG. 1. (Color online) Self-consistent free-electron density in H-like helium for various densities and temperatures. The local free-electron density $n_e(r)$ in units of the average density $N_e = 3Z_f/4\pi R_0^3$ is plotted versus r in units of the Wigner radius R_0 for various plasma-coupling parameters. See text for details.

the ratio R_1/R_0 is proportional to the plasma-coupling parameter

$$R_1/R_0 = \frac{Z_f e^2}{\pi k T_e R_0}, \tag{9}$$

with a definition different by a factor of $1/(\pi Z_f)$ from the most common one, which is based on ion-ion and not electron-ion interaction [9,14]. In this figure, the parameter R_1/R_0 is equal to 1.477×10^{-6}, 1.477×10^{-4}, 0.1477, and 147.7, respectively. Computations performed for $R_1/R_0 = 1.477\times10^4$ have shown that the curve $n_e(r)/N_e$ as a function of r/R_0 is the same as that for $R_1/R_0 = 147.7$ at the drawing accuracy. However, then the use of Fermi-Dirac statistics is required, as discussed in the Appendix. One notes that for $R_1/R_0 \ll 1$ the density varies as $r^{-1/2}$ for small r and stays almost constant for $r \leqslant R_0$. This is close to the behavior predicted by Rosmej *et al.* [28]. For $R_1/R_0 = 0.148$, the electron density varies as $r^{-1/2}$ in almost the whole 0–R_0 region, though one observes a small upward deviation for $r \simeq R_0$. For $R_1/R_0 = 147.7$ the reduced density behaves similarly. Its dependence is again $r^{-1/2}$ in most of the 0–R_0 interval, but for $r \simeq R_0$ there is now a downward deviation.

The radial dependence of the free-electron density is qualitatively similar for higher Z, the main difference being a stronger variation of $n_e(r)$ in the $r = R_0$ region.

Examples of self-consistent calculations of the plasma potential are given in Fig. 2 in H-like aluminum for coupling parameters $R_1/R_0 = 0.01$, 1, and 100. In the numerical

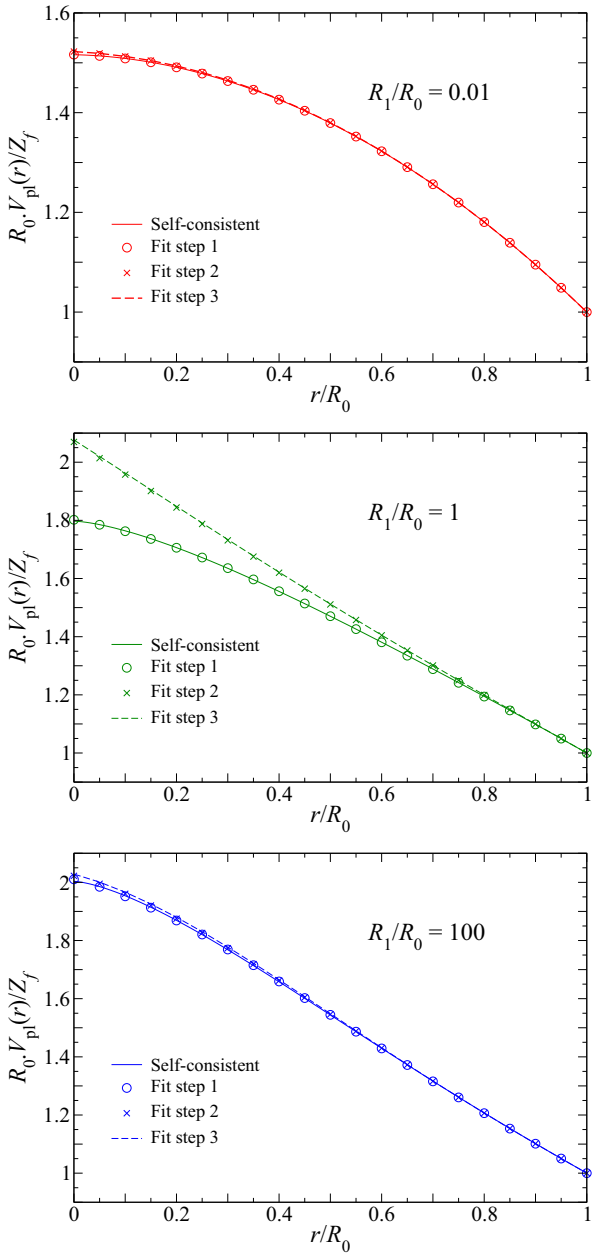

FIG. 2. (Color online) Radial dependence of the self-consistent plasma potential in H-like aluminum, for three values of the coupling parameter, $R_1/R_0 = 0.01$, 1, and 100. The abscissa is the radius in R_0 units; the ordinate is the potential in $Z_f e^2/R_0$ units. The solid line is the numerically obtained self-consistent potential; the circles, crosses, and dashed line are quartic polynomial approximations obtained at three successive steps of the fit discussed in Sec. IV.

integration of the Poisson equation, an integration step $h = 10^{-3}$ was found to provide acceptable accuracy whatever the parameters. For the lowest coupling parameter, the reduced potential almost follows the UEGM law, (7b). We observe that the plasma potential in reduced units $R_0 V_{pl}(r)/Z_f e^2$ changes close to the nucleus by about one-third when the coupling parameter R_1/R_0 increases by 4 orders of magnitude. The three steps in the numerical approximations are described in Sec. IV. Finally, we note that the TF potential in reduced units

is larger than the UEGM potential, as shown by comparison of the upper and lower graphs in Fig. 2.

III. ANALYTICAL PROPERTIES OF THE PLASMA POTENTIAL

A. Scaling laws

From the neutrality, Maxwell-Boltzmann, and Poisson equations, one may easily assert that the reduced potential and free-electron density obey the scaling laws

$$n_e(R_0,R_1,Z,Z_f,r) = Z_f R_0^{-3} f(R_1/R_0,Z,Z_f,r/R_0), \quad (10a)$$

$$V_{\rm pl}(R_0,R_1,Z,Z_f,r) = Z_f R_0^{-1} g(R_1/R_0,Z,Z_f,r/R_0). \quad (10b)$$

If one further assumes that the potential is purely Coulombic, $-Z/r$, these laws even simplify, n_e and $V_{\rm pl}$, depending not independently on Z and Z_f but on the ratio Z/Z_f.

These properties are of interest because they establish that the plots presented in the previous section for the reduced electron density and plasma potential are "universal." Namely, for a given element and charge state, the plots versus the reduced coordinate r/R_0 are the same whatever the temperature and density, provided the parameter R_1/R_0 is conserved.

B. Limit of weakly coupled plasmas

In the limit of infinite temperature or zero density $R_1/R_0 \to 0$, the electron density is constant inside the Wigner sphere and the potential is obtained straightforwardly from the Poisson equation, (7b). This well-known UEGM solution may, however, be usefully refined by considering the first correction in an R_1/R_0 expansion. Starting from the Maxwell-Boltzmann equation, (6a), and the expansion of the incomplete Γ function,

$$\exp(X)\Gamma(3/2,X) = \frac{\sqrt{\pi}}{2} + \frac{\sqrt{\pi}X}{2} - \frac{2X^{3/2}}{3} + \frac{\sqrt{\pi}X^2}{4} + O(X^{5/2}), \quad (11)$$

where the first two terms are kept, one gets, $N_{\rm ht}$ being a normalization constant,

$$n_e(r) = N_{\rm ht}\left\{1 + \frac{e^2}{kT}\left[\frac{Z}{r} - \frac{Z_f}{2R_0}\left(3 - \frac{r^2}{R_0^2}\right)\right]\right\} \quad (12)$$

up to $(R_1/R_0)^{3/2}$ corrections, and the neutrality condition, (2), provides the value of the constant

$$N_{\rm ht} = \frac{3Z_f}{4\pi R_0^3}\frac{1}{1+\frac{3e^2}{2kT_eR_0}\left(Z-\frac{4}{5}Z_f\right)}. \quad (13)$$

From the Poisson integral equation, (5), we write the high-temperature plasma potential

$$V_{\rm pl}^{\rm ht}(r) = \frac{3Z_f e^2/R_0^3}{1+\frac{3e^2}{2kT_eR_0}\left(Z-\frac{4}{5}Z_f\right)} \times\left[\frac{R_0^2}{2} - \frac{r^2}{6} + \frac{Z_f e^2 R_0}{kT_e}\left(\frac{Z}{Z_f} - \frac{5}{8} - \frac{Zr}{2Z_fR_0} + \frac{r^2}{4R_0^2} - \frac{r^4}{40R_0^4}\right)\right] \quad (14)$$

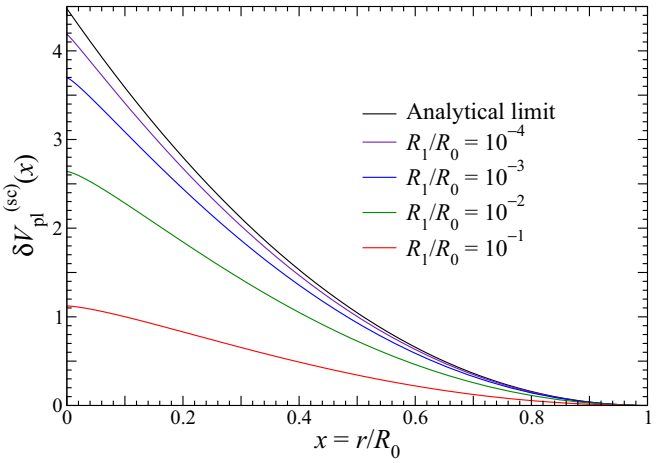

FIG. 3. (Color online) Variation of the reduced plasma potential divided by the coupling parameter R_1/R_0 in H-like helium. The scaled variation $\delta V_{\rm pl}^{\rm (sc)}(x) = (R_0/Z_f e^2)[V_{\rm pl}(r) - V_{\rm pl}^{\rm UEGM}(r)]/(R_1/R_0)$ is plotted versus $x = r/R_0$ for various R_1/R_0 and is compared to the analytical form $y = (3\pi/10)(1-x)^2[5-x-(1-x)^2/4]$ as given by (15b). From bottom to top the various curves correspond to decreasing values of R_1/R_0, the topmost curve being the analytical form.

up to $T_e^{-3/2}R_0^{-5/2}$ terms. Letting

$$u = 1 - r/R_0, \quad (15a)$$

one gets, using the closest-approach distance R_1, (8), the low-density form of the plasma potential, (14):

$$R_0 V_{\rm pl}^{\rm ht}(r)/Z_f e^2 = 1 + u - \frac{u^2}{2} + \frac{3\pi R_1}{10R_0}\left[\left(\frac{5Z}{2Z_f} - 1\right)u^2 + u^3 - \frac{u^4}{4}\right] + O((R_1/R_0)^{3/2}). \quad (15b)$$

This expression only depends on Z/Z_f, R_1/R_0, and r/R_0 as expected.

The convergence of the numerical solution towards this analytical form when the coupling parameter tends to 0 is illustrated in Fig. 3, where we have plotted the radial dependence of the potential variation $(R_0/Z_f e^2)[V_{\rm pl}(r) - V_{\rm pl}^{\rm UEGM}(r)]/(R_1/R_0)$ for various small values of R_1/R_0 and its analytical limit, (14). It turns out that the numerical solution does converge towards this limit but rather slowly with the parameter R_1/R_0, as expected since the first omitted term is of order $(R_1/R_0)^{3/2}$: for instance, if $R_1/R_0 = 10^{-3}$, the analyzed ratio is 3.70, i.e., 17% below the analytical result equal to 4.48.

IV. ANALYTICAL APPROXIMATION FOR THE PLASMA POTENTIAL

The method used to obtain simple analytical approximations of the plasma potential in H-like ions as shown in Fig. 2 will be presented elsewhere, along with an application to energy and rate calculations. Here we only summarize the main results and mention what their usefulness may be in plasma environment studies.

In this work, we focus our attention on the plasma potential and not on the electron density because rather accurate polynomial approximations have been found for the potential, while the electron density behaves close to the nucleus as $r^{-1/2}$. Furthermore, the physical quantities analyzed below, namely, energies, wave functions, transition probabilities, or collisional cross sections, directly depend on this potential and not on the electron density.

An extensive numerical study in H-like ions has shown that that the reduced plasma potential can be rather accurately fitted to the form

$$v_{\rm pl}(r) = R_0 V_{\rm pl}/Z_f e^2 = 2 - r/R_0 + \sum_{i=1}^{n_c} a_i (1 - r/R_0)^{i+1}. \tag{16}$$

This expression ensures that the potential is continuous at $r = R_0$ and that the electric field $\phi(r) = (1/e) dV_{\rm pl}/dr$ has the correct value on the Wigner sphere $\phi(R_0) = -Z_f e/R_0^2$, in agreement with the Gauss theorem and electric neutrality condition. The value $n_c = 3$ was checked to provide a good compromise between accuracy and tractability.

Three determinations have been provided for the coefficients a_i. The first one is based on their direct numerical determination by a linear regression done on the numerically obtained $V_{\rm pl}(r)$. At this step the coefficients a_i depend on the net charge Z_f and on the radii R_0 and R_1, i.e., electronic density and temperature. As mentioned above one considers here only H-like ions, for which $Z_f = Z - 1$. Furthermore, the analysis in the previous section shows that such coefficients are only functions of the "coupling parameter" R_1/R_0 and of the ratio Z_f/Z. Then extensive computations have proven that these coefficients may be reasonably approximated by

$$a_j(\text{step2}) = -\frac{\delta_{j1}}{2} + \frac{R_1/R_0}{M_j R_1/R_0 + P_j}, \tag{17}$$

where δ_{ij} is the Kronecker symbol and the M_j coefficients are determined by linear regression, looking at the dependence of $\rho/(a_j + \frac{\delta_{j1}}{2})$ versus ρ. The P_j coefficients may be derived from the above low-density analysis, (15b):

$$P_1 = \frac{10/3\pi}{5Z/2Z_f - 1}, \quad P_2 = \frac{10}{3\pi}, \quad P_3 = -\frac{40}{3\pi}. \tag{18}$$

The M_j coefficients have to be determined for each Z_f, i.e., for every element, but the above expression holds for any temperature and density. The third step in the fit consists in giving an expression for the M_j coefficients valid for any element. Again, a series of tests leads us to state that a harmonic dependence,

$$M_j = \frac{A_j Z_f + B_j}{C_j Z_f + 1}, \tag{19}$$

provides an acceptable approximation of the numerically derived M_j coefficients. This numerical procedure has led us to the determination

$$A_1 = 0.297\,002, \quad B_1 = 4.217\,15, \quad C_1 = 0.309\,115, \tag{20a}$$

$$A_2 = 1.345\,74, \quad B_2 = 10.917, \quad C_2 = 0.903\,015, \tag{20b}$$

$$A_3 = -0.714\,927, \quad B_3 = -7.189\,77, \quad C_3 = 0.601\,471, \tag{20c}$$

where the nonlinear fit was performed using a standard Mathematica routine.

An example of the calculation of the plasma potential and of the three steps in the numerical fit is given in Fig. 2. It appears that the first step in the procedure is always very accurate. The second and third steps are in very good agreement and differ significantly—but by less than 30% and, in most cases, less than 15%—from the self-consistent TF potential in the intermediate case $R_1/R_0 \simeq 1$. In conclusion, the proposed approximations are fair whatever the coupling parameter is, the only exception being when this parameter is close to 1 in the second and third steps of the fit.

V. ENERGIES AND RADIATIVE RATES

When the plasma potential analyzed in the previous sections is included in the Hamiltonian, the ion energies and wave functions are modified. In a previous paper [15], we have shown how to include this potential in the UEGM limit in the FAC [16]. The same procedure may be applied with the TF potential. This refined potential may also be included in analytical calculations for H-like ions.

In Fig. 4, the binding energy of Al XIII for the $1s_{1/2}$ level is plotted versus the temperature. We compare in that graph the binding energy of the isolated ion, the UEGM, and the TF approach, which is the only model dependent on the temperature. Here and in the following we consider a specific charge state without consideration of the real ionization degree that would be reached under these thermodynamic conditions. We clearly see that the binding energy increases with the temperature in the TF case. We also verify that, as expected, at high temperatures, the TF approach converges with the UEGM.

As the above analysis of the plasma potential has shown, the TF potential is always greater than the UEGM potential. Therefore one expects that the binding energy will be lower with the TF model than with the UEGM. Indeed, Fig. 5 confirms this prediction. An important point to highlight in Figs. 4 and 5 is that the most important effect on the level shift originates from the density and not the temperature. Our

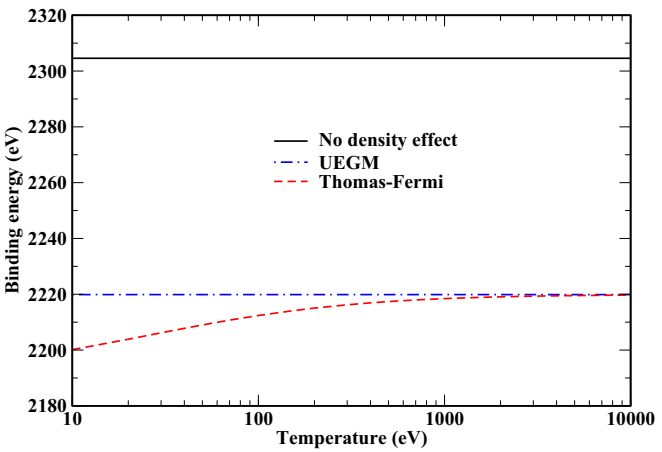

FIG. 4. (Color online) Influence of temperature on the binding energy of Al XIII for the $1s_{1/2}$ level with an average density $N_e = 10^{23}$ cm^{-3}.

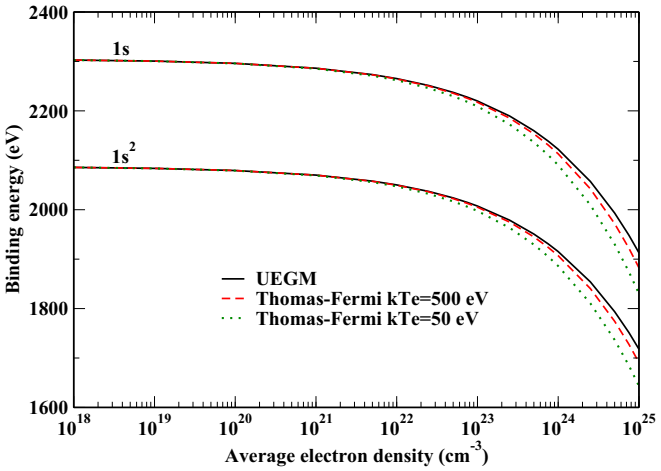

FIG. 5. (Color online) Influence of density on the binding energy of Al XIII and XII for the $1s_{1/2}$ (upper group) and $1s^2\,{}^1S_0$ (lower group) levels.

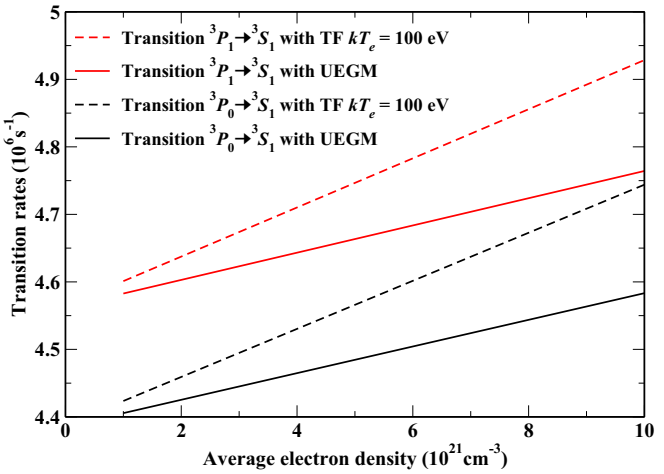

FIG. 7. (Color online) Dipolar radiative rates $1s4p\,{}^3P_J \rightarrow 1s4s\,{}^3S_1$ in Al XII versus the average electron density at $T_e = 100$ eV. Gray (red) lines correspond to $J = 1$; black lines, to $J = 0$.

results are at variance with Salzmann and Szichman's [17], who obtained, in some cases, a UEGM shift greater than the TF shift.

Generally speaking, we cannot assert whether dipolar radiative rates are decreasing or increasing with density. Such behavior has been mentioned previously by Li and Rosmej [30]. This is because such rates depend on transition energies and dipolar matrix elements, and as may be seen, for instance, in Fig. 6, the transition energy may increase or decrease with the density. Specifically, the transition energy decreases with the density between the triplet $^3P_{0,1}$ and the singlet $^1S_0$—at least before the level crossing at $\sim 3\times10^{22}$ cm^{-3}—and increases between the triplet $^3P_{0,1}$ and the triplet $^3S_1$. Thus radiative rates may exhibit different behaviors with respect to the density. In a similar way, Fig. 7 shows that radiative rates between the triplet $^3P_{0,1}$ and the singlet $^1S_0$ of Al XII increase with the density. However, as shown in Fig. 8 the $1s$–$2p_j$ rates decrease in the case of hydrogen-like Al. In both cases the UEGM leads to a qualitatively similar behavior but a smaller change in the radiative rates.

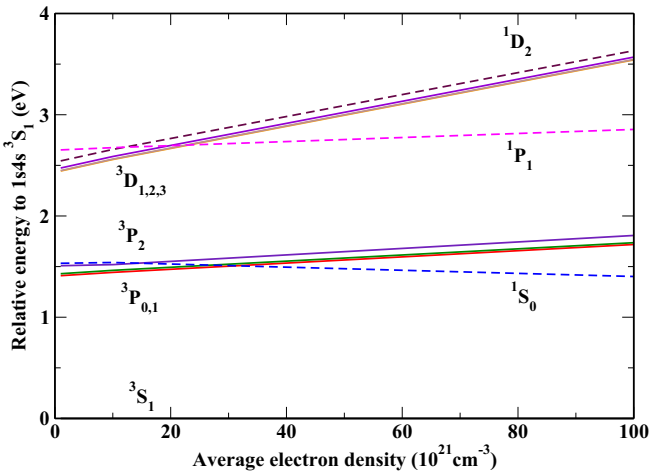

FIG. 6. (Color online) Energy of helium-like Al relative to the level $1s4s\,{}^3S_1$ versus density for various levels of the configuration $1s4l$. Plasma density effects are accounted for using a Thomas-Fermi potential at 100 eV. The three curves associated with the ^3D term are almost identical, with similar overlapping for the two curves associated with the $^3P_0$ and $^3P_1$ levels.

VI. EXCITATION CROSS SECTIONS

As mentioned previously, there exists an abundant literature on density effects on collisional cross sections. However, a series of papers uses the Debye-Hückel theory, which, as stated by Nguyen *et al.* [18], is not well suited for strongly coupled plasmas. Besides, as mentioned by Whitten *et al.* [24], in some cases even the zero-density cross sections are not correct: in Ref. [21], the cross sections are multiplied by the initial level degeneracy.

We use two methods to study excitation cross sections: the Born approximation and distorted waves (DWs)

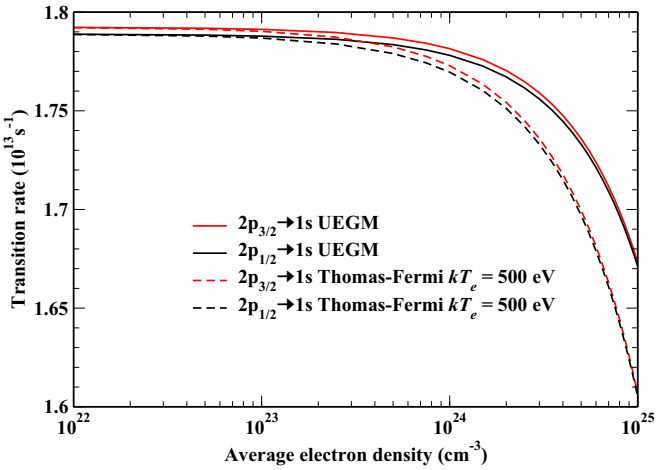

FIG. 8. (Color online) Dipolar radiative rates in Al XIII versus the average electron density at $T_e = 500$ eV. Gray (red) curves represent the $2p_{3/2} \rightarrow 1s$ rates; black curves, the $2p_{1/2} \rightarrow 1s$ rates.

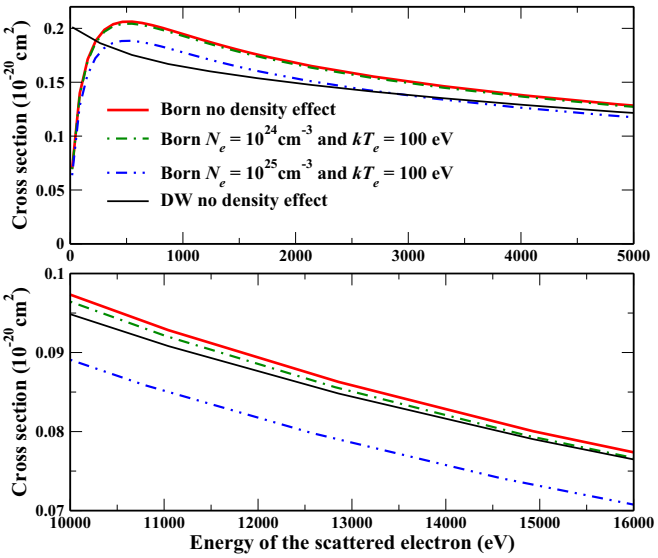

FIG. 9. (Color online) Comparison of excitation cross sections for the $1s$–$2p_{1/2}$ transition for Al XIII at several densities and $T = 100$ eV.

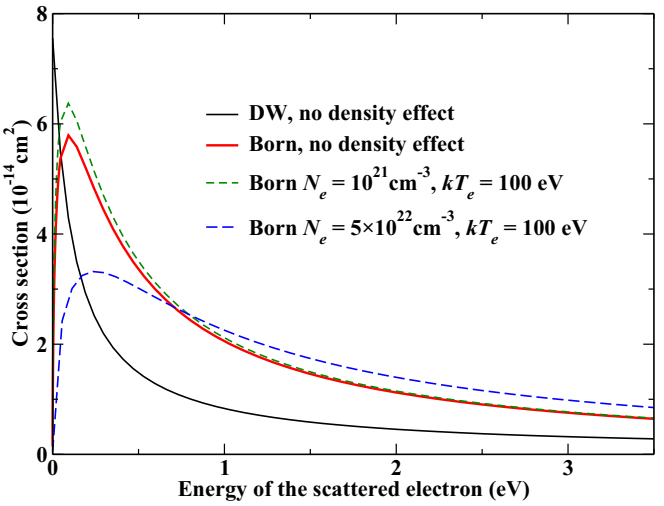

FIG. 10. (Color online) Comparison of excitation cross sections for the transition between $1s4d\ ^1D_2$ and $1s4p\ ^1P_1$ for Al XII at several densities.

(see Chap. 3 in [31]). The selection of the proper method requires consideration of which asymptotic behavior these formalisms assume for the long-range potential. Both of them are perturbative theories and valid only in the case of a weak interaction potential between the target and the incident electrons. The differences, however, are important. The DW method takes into account the long-range form of the potential, contrary to the Born approximation. The form of the incident particle wave function is a plane wave for the Born approximation and Coulombic for DWs. These differences mean that the distorted wave method should give good results for an ion, whereas the Born approximation should give good results for neutral atoms or for an incident particle at high energy. So, the DW model is not relevant when density effects in the ion-sphere model are considered, because the asymptotic potential is not Coulombic.

We must emphasize a difficulty met when one tries to observe the influence of the plasma on cross sections. Indeed, the effect of the plasma will change the long-range behavior of the potential. Without plasma the asymptotic potential is that of an ion, and with plasma, due to neutrality inside the Wigner-Seitz sphere, that of a neutral atom. However, at high energies the DW and Born approximation converge, meaning that we can then isolate the influence of plasma.

In order to compare the Born approximation to DW results we have plotted in Fig. 9 the e-impact excitation cross sections for the $1s$–$2p_{1/2}$ transition in Al XIII. Since, as mentioned above, the DW theory is not adapted when density effects are accounted for, such effects have been included in the Born theory only.

The behavior of the cross sections from both methods is different near threshold due to the way they treat long-range interactions. Nevertheless, at high energies, cross sections show the same behavior. In Fig. 9 we note that the plasma effect lowers this excitation cross section, though this variation is minor. To observe a significant change, we have to reach a high density such as $N_e = 10^{25}$ cm^{-3}. Then one has for the Wigner radius $R_0 = 1.25a_0$, which is much larger than the wave-function extension, and the "plasma coupling parameter" $Z_f e^2/kTR_0 = 2.62$. This means that our formalism assuming nonoverlap conditions of ion wave functions [15] is applicable, while non-negligible density effects occur.

As seen in Sec. V, the radiative rates may increase or decrease depending on the studied transition, and the same behavior applies to excitation cross sections. Indeed excitation cross sections may increase as shown in the Al XII case presented in Fig. 10. In that case the transition energy from $1s4p\ ^1P_1$ to $1s4d\ ^1D_2$ first decreases with density, and at the density $N_e \simeq 1.2\times10^{22}$ cm^{-3} these levels cross. We observe in Fig. 10 that the cross section increases until this critical density is reached. After the crossing the emission occurs from $^1D_2$ to $^1P_1$ and the cross section decreases with the density. The increase in the cross section is stronger around the peak, but we have to keep in mind that the Born calculation overestimates the cross section in this area. Thus we must only rely on the high-energy results where the cross-section shift is small.

We use the Van Regemorter formula [32] to confirm our observations. This formula is valid under the Born approximation and Bethe assumption (high energy and dipolar transition),

$$\sigma_{ij} = \frac{8\pi}{\sqrt{3}}\frac{R_y^2}{e_i}\frac{f_{ij}}{\Delta E_{ij}}\bar{g}(e_i/\Delta E_{ij})\pi a_0^2, \tag{21}$$

where ΔE_{ij} is the transition energy from level i to level j, a_0 the Bohr radius, R_y the Rydberg energy, e_i the energy of the incident electron, $\bar{g}$ the Gaunt factor determined through empirical observations, and f_{ij} the oscillator strength. We choose the Gaunt factor as suggested by Mewe [33]:

$$\bar{g} = 0.15 + 0.28\ln\left(\frac{e_i}{\Delta E_{ij}}\right). \tag{22}$$

We compare numerical cross sections and the Van Regemorter formula in Fig. 11. We note that the shift of cross sections is similar. In order to provide analytical expressions for the cross sections in the simplest case, we use a development

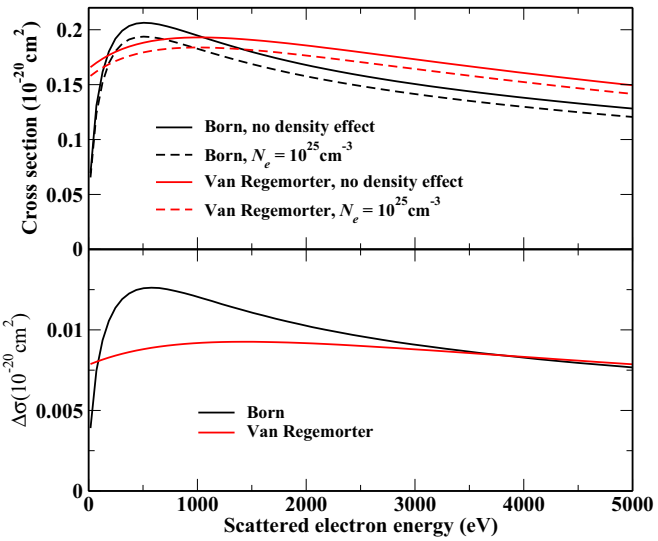

FIG. 11. (Color online) Excitation cross sections for the transition $1s_{1/2}$–$2p_{1/2}$ in Al XIII: comparison between the Born approximation and the Van Regemorter formula. Top: Cross sections. Bottom: Variations $\sigma(N_e = 0) - \sigma(N_e > 0)$ for both approximations. The plasma effect is accounted for within the UEGM. The Born data are shown in black; the Van Regemorter data, in gray (red).

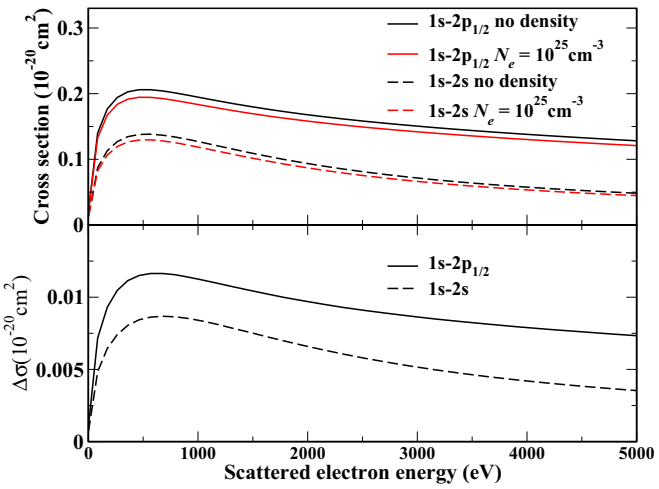

FIG. 12. (Color online) Comparison of excitation cross sections for the transitions $1s$–$2p_{1/2}$ (dashed lines) and $1s_{1/2}$–$2s_{1/2}$ (solid line) for Al XIII using the Born approximation. When density effects are included, the Thomas-Fermi model is used, with a temperature of 500 eV. Top: Black (upper) curves represent cross sections without density effects, while gray (red; lower) curves represent cross sections at $N_e = 10^{25}$ cm^{-3}. Bottom: Variations $\sigma(N_e = 0) - \sigma(N_e > 0)$ for both transitions.

based on Eq. (21). In that equation, the density effects modify the transition energy ΔE_{ij} and the oscillator strength f_{ij}. The Gaunt factor is also modified but we neglect it because of its slow variation with ΔE_{ij}. Thus the magnitude of the cross section mainly depends on the ratio $f_{ij}/\Delta E_{ij}$. Up to numerical constants this ratio is the square of a matrix element,

$$\frac{f_{ij}}{\Delta E_{ij}} \propto \langle n_i l_i \,|r|\, n_j l_j\rangle^2. \tag{23}$$

In a previous work [15], we have developed analytical formulas for hydrogen-like ions in the UEGM framework. Thanks to this, we are able to isolate the contribution of the plasma potential by decomposing the matrix element at the zeroth and first orders of perturbation:

$$\langle n_i l_i|r|n_j l_j\rangle = \langle n_i l_i|r|n_j l_j\rangle^0 + \widetilde{\langle n_i l_i|r|n_j l_j\rangle}. \tag{24}$$

We calculate the matrix element under the UEGM for the nonrelativistic transition $1s$–$2p$ and obtain, for a hydrogen-like ion, in atomic units

$$\langle 1s\,|r|\,2p\rangle = \frac{128}{243}\frac{\sqrt{6}}{Z}\left(1 - \frac{3059}{36}\frac{Z_f}{Z^4 R_0^3}\right). \tag{25}$$

In the case of hydrogen-like Al, we get

$$\langle 1s\,|r|\,2p\rangle^0 = 9.925\times10^{-2}, \tag{26}$$

and for an average free-electron density $N_e = 10^{24}$ cm^{-3},

$$\widetilde{\langle 1s\,|r|\,2p\rangle} = -1.8329\times10^{-4}. \tag{27}$$

At such a density the matrix-element perturbation is very small. Equations (26) and (27) confirm that the excitation cross section is not notably modified.

Forbidden and allowed transitions are differently affected by the plasma potential. This comparison is illustrated in Fig. 12, where cross sections are calculated via the Born approximation. The plot clearly shows that the allowed transition $1s - 2p_{1/2}$ is more sensitive to the plasma potential than the forbidden transition $1s - 2s$. This result was first observed and explained by Hatton *et al.* [22], who used a different plasma potential (Debye potential).

As shown in Figs. 9–11, usually the cross sections decrease with the plasma density. This can be checked directly with the Van Regemorter formula, (21), since the ratio $f_{ij}/\Delta E_{ij}$ is proportional to the squared radial matrix element, which usually decreases with density. Accordingly, in the cases considered in [15], hydrogenic radiative rates decrease with the plasma density, while the present Fig. 7 provides a specific example where rates increase with density. Here we may check quantitatively that the variation of the excitation cross sections and of the radiative rates are of the same sign and that the latter is usually greater in magnitude. This is illustrated in the H-like Al case at $N_e = 10^{25}$ cm^{-3} in Tables I and II for the Born cross sections and the rates, respectively.

However, the collisional excitation *rates* are affected differently by the plasma environment. Assuming a

TABLE I. Relative variation of the collisional excitation cross section for the $1s$–$2p_{1/2}$ transition in Al XIII using the Born approximation. The difference $\sigma(N_e, E_f)/\sigma(N_e = 0, E_f) - 1$ is detailed for various outgoing electron energies E_f and various plasma-density models assuming $N_e = 10^{25}$ cm^{-3}.

	Thomas-Fermi			
E_f (eV)	$T_e = 100$ eV	$T_e = 500$ eV	$T_e = 2000$ eV	UEGM
500	−0.085	−0.060	−0.0489	−0.0426
2000	−0.086	−0.061	−0.0494	−0.0430

TABLE II. Relative variation $X(N_e)/X(N_e=0)-1$ of the radiative (A) and collisional-excitation rates (R) for the $1s$–$2p_{1/2}$ transition in Al XIII. Collisional rates are computed using the Born approximation. The electronic density is $N_e = 10^{25}$ cm^{-3}. The collisional-excitation rate variation within the UEGM is computed at $T_e = 100$ eV; at $T_e = 2000$ eV this variation would be -0.040.

	Thomas-Fermi		
	$T_e = 100$ eV	$T_e = 2000$ eV	UEGM
$\Delta A/A$	-0.147	-0.080	-0.066
$\Delta R/R$	$+0.324$	-0.045	$+0.095$

TABLE III. Relative variation $X(N_e)/X(N_e=0)-1$ of the radiative (A) and Born collisional-excitation rates (R) for the $1s4d\ ^1D_2$–$1s4p\ ^1P_1$ transition in Al XII. The electronic density is $N_e = 10^{21}$ cm^{-3}. The collisional-excitation rate variation within the UEGM is computed at $T_e = 5$ eV; at $T_e = 100$ eV this variation would be -0.0059.

	Thomas-Fermi		
	$T_e = 5$ eV	$T_e = 100$ eV	UEGM
$\Delta A/A$	-0.39	-0.16	-0.086
$\Delta R/R$	$+0.044$	$+0.0116$	$+0.0082$

Maxwell-Boltzmann distribution for the free electrons, the collisional excitation rate for the $i \to j$ transition is

$$R_{ij} = \frac{(2\pi)^{1/2}\hbar^2 N_e}{g_i (m_e k T_e)^{3/2}} \times \exp\left(-\frac{\Delta E_{ij}}{kT_e}\right) \int_0^\infty \Omega_{ij}(e_f) \exp(-e_f/kT_e)\, de_f, \tag{28}$$

where e_f is the scattered electron energy and $\Omega_{ij}(e_f)$ the collision strength,

$$\Omega_{ij}(e_f) = \frac{2 m_e g_i}{\pi\hbar^2}(e_f + \Delta E_{ij})\sigma_{ij}. \tag{29}$$

For low T_e, the integral over e_f in the rate, (28), tends to $kT_e\Omega_{ij}(0)$, simply proportional to the collision strength at threshold. Therefore, the ratio of the excitation rates with and without the plasma effect is

$$R_{ij}^{\rm pl}/R_{ij}^{(0)} = \exp\left(-\frac{\Delta E_{ij} - \Delta E_{ij}^{(0)}}{kT_e}\right) \Omega_{ij}(0)/\Omega_{ij}^{(0)}(0) \quad \text{if} \quad kT_e \ll \Delta E_{ij}. \tag{30}$$

Since, as we have seen, the difference $\Delta E_{ij} - \Delta E_{ij}^{(0)}$ is, in most cases, negative, the first factor in the ratio, (30), is greater than 1 and increases with $1/T_e$, while the ratio of the collision strengths at threshold, though less than 1, does not depend on T_e within the UEGM or slowly varies with T_e in the TF hypothesis. Therefore for low enough T_e the collisional excitation rate *increases* when the plasma effect is accounted for. One should note that the above analysis does not rely on any approximation on atomic structure or scattering theory but on the general behavior of the plasma effect on transition energies and collision strengths. The opposite case of large T_e can be investigated using the Van Regemorter formula, (21), from which one gets the rate

$$R_{ij}|_{\rm VR} = \frac{16\pi\sqrt{2} R_y^2 \pi^2 a_0^2 N_e f_{ij}}{(3\pi m_e k T_e)^{1/2}\Delta E_{ij}}\, \bar{g}\left(\frac{\Delta E_{ij}}{kT_e}\right) \exp\left(-\frac{\Delta E_{ij}}{kT_e}\right). \tag{31}$$

Since the variation of the Gaunt factor with the plasma effect can usually be neglected, the effect of the plasma environment for large T_e is measured by the ratio

$$R_{ij}^{\rm pl}/R_{ij}^{(0)}|_{\rm VR} = \exp\left(-\frac{\Delta E_{ij} - \Delta E_{ij}^{(0)}}{kT_e}\right) \frac{f_{ij}/\Delta E_{ij}}{f_{ij}^{(0)}/\Delta E_{ij}^{(0)}} \quad \text{if} \quad kT_e \gg \Delta E_{ij}. \tag{32}$$

As mentioned above, (23), the ratio $f_{ij}/\Delta E_{ij}$ is proportional to a squared dipolar matrix element and usually decreases when the plasma effect is accounted for—though we have seen previously [15] that the opposite may be true. Conversely, as mentioned when discussing Eq. (30), the ratio of the Boltzmann factors increases when the plasma effect is included. Therefore the ratio, (32), may be less than or greater than 1 and usually increases with $1/T_e$. These considerations are illustrated in the last row in Table II, where we may verify that for the $1s$–$2p$ transition in H-like aluminum the plasma environment effect increases the collisional excitation rates at low temperatures, while it lowers these rates at high temperatures. In the considered case this behavior is at variance with the plasma effect on the radiative rate.

The rates for the $1s4d\ ^1D_2$-to-$1s4p\ ^1P_1$ transition in He-like aluminum are analyzed in Table III. Once again, the radiative rate decreases when the density effect is included: this arises from the decrease in the transition energy, which is particularly strong here since the levels cross at $N_e \simeq 1.2\times10^{22}$ cm^{-3}. At the density considered in this table, the collisional rates increase when the environment effect is accounted for, whatever the temperature: this behavior is related to the above-mentioned increase in the cross sections (Fig. 10).

VII. IONIZATION CROSS SECTIONS

Several works have considered the influence of the plasma environment on electron-impact ionization cross sections. Some use the Debye-Hückel theory (e.g., [23]); others, theTF approach [27]. Both the cited works use the Hartree-Fock-Slater theory with cross sections computed using DWs. Here we have adopted the TF formalism for the plasma effect, but the collision formalism used, instead of DWs, is the more relevant binary encounter dipole (BED) theory [34] implemented in the FAC. This method combines the Mott semiclassical calculation of the cross section [35] for the scattering of two free electrons (valid for close collisions, i.e., at large momentum transfer) and the Bethe theory [36], which is the Born plane-wave approximation (valid at high energy and small momentum transfer) with only the dipolar term kept. This theory is of great interest due to its applicability for both ions and neutral atoms. Contrary to the case of excitation, we do not need to change our calculation approach when the plasma effect is included.

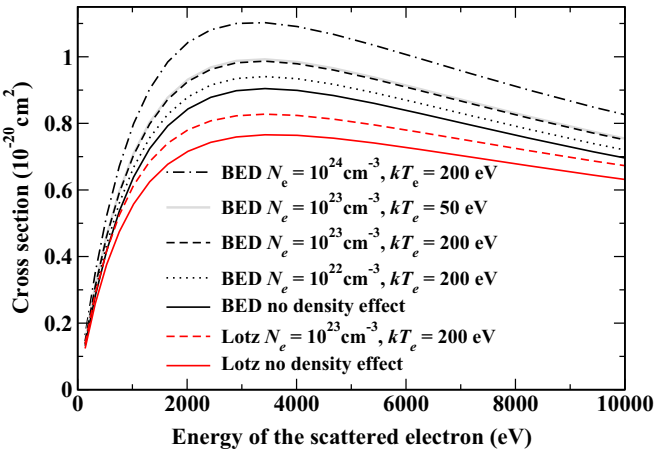

FIG. 13. (Color online) Comparison of ionization cross sections for the transition $1s^2$ to $1s$ for Al XII at $T = 200$ eV (and 50 eV) for $N_e = 10^{23}$ cm^{-3}. The free-electron density is obtained from the Thomas-Fermi model, and for the scattering process the BED and Lotz formalisms are compared. Grayscale version: the curves are in the same order in the graph and in the legend.

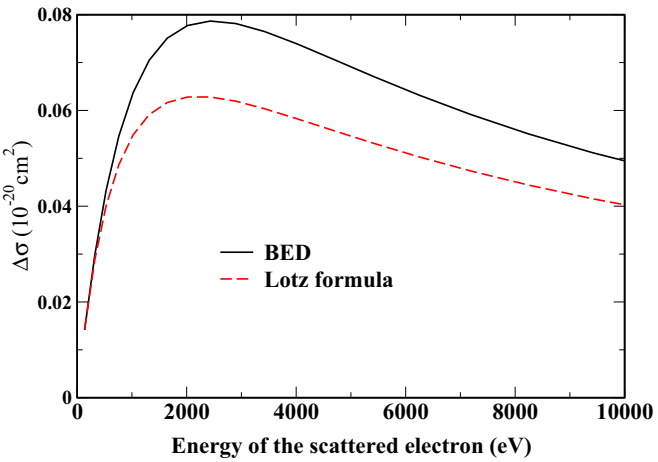

FIG. 14. (Color online) Modification of the ionization cross section due to the density effect for the transition $1s^2$ to $1s$ in Al XII obtained using the BED theory or Lotz formula. The plotted quantities are the cross sections at $N_e = 10^{23}$ cm^{-3} and $T = 200$ eV minus the cross sections at $N_e = 0$ cm^{-3}.

We plot the electron-impact-ionization cross sections from state $1s^2$ to state $1s$ in Al, at several densities, in Fig. 13. A comparison is done with the empirical Lotz formula [37]

$$\sigma_{ij} = C\pi a_0^2 Ry^2 \frac{w_n}{e_i \Delta E_{ij}} \ln\left(\frac{e_i}{\Delta E_{ij}}\right), \tag{33}$$

where $C = 2.77$ and w_n is the initial number of electrons concerned by the ionization process in the shell.

Our purpose is not to discuss the accuracy of the Lotz formula compared to the BED method, but to characterize the plasma effect. The cross section increases with the density, as shown in Fig. 13. We can explain this increase by the decrease in the transition energy, which in turn leads to a larger collisional ionization. When we compare the cross-section variation due to the plasma effect at $N_e = 10^{23}$ cm^{-3} and $T_e = 200$ eV for the BED and Lotz formulas in Fig. 14, we note that they are quite similar. We also see in this plot that the cross-section variation increases with the energy of scattered electrons and then slowly decreases after the peak. The temperature has an effect opposite to that of the density: when it increases the cross section decreases.

We can support these results using a formalism based on the Lotz formula and a perturbative approach within the UEGM. As mentioned above, in the UEGM, the first-order energy correction for a hydrogen-like ion is, in atomic units,

$$E^{(1)}_{\text{plasma}} = \frac{Z_f}{R_0}\left(\frac{3}{2} - \frac{\langle r^2\rangle_{nl}}{2R_0^2}\right), \tag{34}$$

with

$$\langle r^2\rangle_{nl} = \frac{n^2}{2Z^2}(5n^2 - 3l(l+1) + 1). \tag{35}$$

For example, for the ionization of a hydrogen-like ion in the nl state to a fully stripped ion, the transition energy is

$$\Delta E = \frac{Z^2}{2n^2} - \frac{Z_f}{R_0}\left(\frac{3}{2} - \frac{\langle r^2\rangle_{nl}}{2R_0^2}\right), \tag{36}$$

which shows that the energy decreases with the density. The cross section increases with density due to its dependence on the energy transition $1/\Delta E_{ij}$, as shown in Fig. 13. The study on other elements leads to the same results.

Our results agree with those of Wu *et al.* [27] in the increase in the ionization cross section with density, though their work relies on DW theory. As mentioned by Pindzola *et al.* [23], we checked that their cross sections in Ge-like gold are underestimated by a factor of 2. But the cross sections from [23] decrease with the density. These authors explain that this behavior is linked to the Debye screening of interelectronic interaction. However, their work, since it is based on Debye theory, is applicable only at low coupling parameters, while we do not believe that the same restriction applies to the present work. Additional results from theory and experiment would be useful to clarify this point.

VIII. SUMMARY AND CONCLUSIONS

Using a TF approach for free electrons, we have investigated the effect of the plasma environment on the atomic structure. It has been shown that this formalism, valid at finite temperature, leads to a larger plasma potential than the UEGM previously used. In most cases the inclusion of density effects results in level shifts and changes in rates, which are stronger with the TF model than with the UEGM. This is related to the magnitude of the plasma potential, which is larger in the TF model than in the UEGM. This self-consistent plasma potential has been included in the FAC, allowing us to obtain an accurate atomic description for opacity calculations or collisional-radiative models. The results obtained here show that no general behavior for the perturbation of bound-bound processes can be predicted. As a spectroscopic analysis by Li and Rosmej [30] has shown, transition energies may increase or decrease with the electron density. Using the FAC we have been able to confirm this observation and have generalized it to radiative rates and e-impact excitation rates. The situation is usually simpler for H-like ions, as stated

previously [15]. In the case of the $1s4l$ configuration of helium-like aluminum, we obtained ionization cross sections increasing with density, a fact which we explained by the decrease in the transition energy. Furthermore, it has been shown that, at low temperatures, the collisional-excitation rates usually increase when the plasma environment effect is accounted for, while the radiative rates usually decrease. This should have important consequences for population kinetics in plasmas out of local thermodynamical equilibrium.

This work represents a first important step in the investigation of density effects in a collisional-radiative code. Indeed, a previous study [38] using a plasma potential based on quasiparticle energies and effective interaction argues that the plasma environment has a minor impact on parameters such as the average charge. However, this work clearly shows that atomic processes are perturbed in a non-negligible way. Therefore it is highly desirable to investigate environment effects on plasma kinetics, as well as on absorption and emission spectra.

ACKNOWLEDGMENTS

This work was partly supported by the European Communities under the contract of association between EURATOM and CEA within the framework of the European Fusion Program.

APPENDIX: PLASMA POTENTIAL IN THE CASE OF DEGENERATE ELECTRONS

Defining the thermal wavelength as $\lambda_{\rm th} = h/(2\pi m k_{\rm B} T_e)^{1/2}$, the nondegeneracy condition is written

$$g = N_e \lambda_{\rm th}^3 = \frac{3\pi^2}{(2Z_f)^{1/2}} \frac{(a_0 R_1)^{3/2}}{R_0^3} \ll 1 \qquad \text{(A1)}$$

using the Wigner radius and closest-distance approach, (8). The difference between Maxwell-Boltzmann and Fermi-Dirac statistics is illustrated in Fig. 15, where we have plotted the numerical results for the free-electron density and plasma potential in the case of H-like aluminum at 1 eV and 10^{24} e/cm^3. In this case the degeneracy factor $g = N_e \lambda_{\rm th}^3$ is 331 and the plasma coupling parameter is $\Gamma = \pi R_1/R_0 = 121.7$, making the free electrons degenerate. However, one notes in this figure that the relative variation between Maxwell-Boltzmann and Fermi-Dirac statistics is about 0.2 for the density and 0.1 for the potential. If one considers the relative variation of the potential versus the UEGM limit, the modification due to quantum statistics is again 0.2.

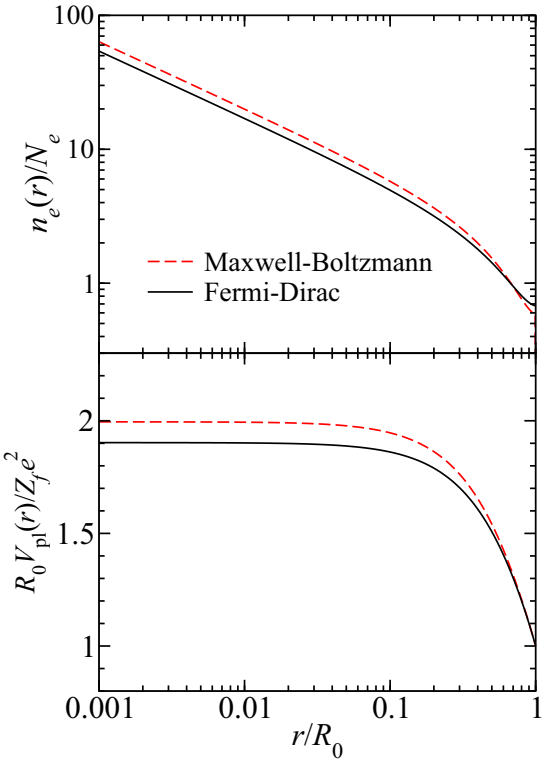

FIG. 15. (Color online) Influence of statistics on the self-consistent free-electron density and plasma potential for H-like aluminum at $T_e = 1$ eV and $N_e = 10^{24}$ cm^{-3} or 0.148 a_0^{-3}. The density is in units of the average free-electron density $N_e = 3Z_f/4\pi R_0^3$, the potential energy is in units of $Z_f e^2/R_0$, and the electronic distance to nucleus r is in units of the Wigner sphere radius $R_0 = 2.684\, a_0$.

Accordingly, in Fig. 5, the most degenerate case considered was $T_e = 50$ eV, $N_e = 10^{25}$ cm^{-3}, for which the degeneracy factor is $g \sim 9.36$, therefore suggesting that Fermi-Dirac statistics should be used. An analysis similar to the one above has shown that the difference in the plasma potential is also below 10%, and this corresponds to the maximum degeneracy parameter. Indeed $N_e = 10^{25}$ cm^{-3} is well above solid density, so the approximation done using the ion-sphere model is much cruder than that on the statistics. This is why we only consider Maxwell-Boltzmann statistics in this work.

[1] H. R. Griem, *Principles of Plasma Spectroscopy*, *Cambridge Monographs on Plasma Physics* (Cambridge University Press, Cambridge, UK, 2005).
[2] M. Baranger, Phys. Rev. **112**, 855 (1958).
[3] B. F. Rozsnyai, Phys. Rev. A **43**, 3035 (1991).
[4] P. Debye and E. Hückel, Phys. Z. **24**, 185 (1923).
[5] D. A. Liberman, Phys. Rev. B **20**, 4981 (1979).
[6] R. P. Feynman, N. Metropolis, and E. Teller, Phys. Rev. **75**, 1561 (1949).
[7] B. F. Rozsnyai, Phys. Rev. A **5**, 1137 (1972).
[8] M. W. C. Dharma-wardana and F. Perrot, Phys. Rev. A **26**, 2096 (1982).
[9] S. Ichimaru, Rev. Mod. Phys. **54**, 1017 (1982).
[10] T. Blenski and B. Cichocki, Phys. Rev. E **75**, 056402 (2007).
[11] R. Piron and T. Blenski, Phys. Rev. E **83**, 026403 (2011).
[12] T. Blenski, R. Piron, C. Caizergues, and B. Cichocki, High Energy Density Phys. **9**, 687 (2013).
[13] J. C. Stewart and K. D. Pyatt, Jr., Astrophys. J. **144**, 1203 (1966).

[14] J. C. Weisheit, in *Applied Atomic Collision Physics Vol. 2*, edited by H. S. W. Massey, E. W. Mc Daniel, and B. Bederson (Academic Press, Orlando, FL, 1984).
[15] M. Belkhiri and M. Poirier, High Energy Density Phys. **9**, 609 (2013).
[16] M. F. Gu, Can. J. Phys. **86**, 675 (2008).
[17] D. Salzmann and H. Szichman, Phys. Rev. A **35**, 807 (1987).
[18] H. Nguyen, M. Koenig, D. Benredjem, M. Caby, and G. Coulaud, Phys. Rev. A **33**, 1279 (1986).
[19] S. Bhattacharyya, A. N. Sil, S. Fritzsche, and P. K. Mukherjee, Eur. Phys. J. D **46**, 1 (2008).
[20] D. P. Kilcrease, R. C. Mancini, and C. F. Hooper, Phys. Rev. E **48**, 3901 (1993).
[21] J. Davis and M. Blaha, J. Quant. Spectrosc. Radiat. Transfer **27**, 307 (1982).
[22] G. J. Hatton, N. F. Lane, and J. C. Weisheit, J. Phys. B **14**, 4879 (1981).
[23] M. S. Pindzola, S. D. Loch, J. Colgan, and C. J. Fontes, Phys. Rev. A **77**, 062707 (2008).
[24] B. L. Whitten, N. F. Lane, and J. C. Weisheit, Phys. Rev. A **29**, 945 (1984).
[25] M. C. Zammit, D. V. Fursa, and I. Bray, Phys. Rev. A **82**, 052705 (2010).
[26] M. Schlanges and T. Bornath, Physica A **192**, 262 (1993).
[27] Z. Q. Wu, G. X. Han, J. Yan, and J. Q. Pang, J. Phys. B **35**, 2305 (2002).
[28] F. Rosmej, K. Bennadji, and V. S. Lisitsa, Phys. Rev. A **84**, 032512 (2011).
[29] M. Abramowitz and I. Stegun, *Handbook of Mathematical Functions* (National Bureau of Standards, Washington, DC, 1972).
[30] X. Li and F. B. Rosmej, Phys. Rev. A **82**, 022503 (2010).
[31] I. I. Sobel'man, L. A. Vainshtein, and E. A. Yukov, *Excitation of Atoms and Broadening of Spectral Lines* (Springer, Berlin, 1995).
[32] H. Van. Regemorter, Astrophys. J. **136**, 906 (1962).
[33] R. Mewe, Astron. Astrophys. **20**, 215 (1972).
[34] Y.-K. Kim and M. E. Rudd, Phys. Rev. A **50**, 3954 (1994).
[35] N. F. Mott, Proc. R. Soc. London Ser. A **126**, 259 (1930).
[36] H. Bethe, Ann. Phys. (Leipzig) **397**, 325 (1930).
[37] W. Lotz, Z. Phys. **206**, 205 (1967).
[38] C. A. Iglesias and R. W. Lee, J. Quant. Spectrosc. Radiat. Transfer **58**, 637 (1997).